

# Development of Dual PZT Transducers for Reference-Free Crack Detection in Thin Plate Structures

Hoon Sohn and Seuno Bum Kim

**Abstract**—A new Lamb-wave-based nondestructive testing (NDT) technique, which does not rely on previously stored baseline data, is developed for crack monitoring in plate structures. Commonly, the presence of damage is identified by comparing “current data” measured from a potentially damaged stage of a structure with “baseline data” previously obtained at the intact condition of the structure. In practice, structural defects typically take place long after collection of the baseline data, and the baseline data can be also affected by external loading, temperature variations, and changing boundary conditions. To eliminate the dependence on the baseline data comparison, the authors previously developed a reference-free NDT technique using 2 pairs of collocated lead zirconate titanate (PZT) transducers placed on both sides of a plate. This reference-free technique is further advanced in the present study by the necessity of attaching transducers only on a single surface of a structure for certain applications such as aircraft. To achieve this goal, a new design of PZT transducers called dual PZT transducers is proposed. Crack formation creates Lamb wave mode conversion due to a sudden thickness change of the structure. This crack appearance is instantly detected from the measured Lamb wave signals using the dual PZT transducers. This study also suggests a reference-free statistical approach that enables damage classification using only the currently measured data set. Numerical simulations and experiments were conducted using an aluminum plate with uniform thickness and fundamental Lamb waves modes to demonstrate the applicability of the proposed technique to reference-free crack detection.

## I. INTRODUCTION

FOR structural health monitoring (SHM) and nondestructive testing (NDT) of plate structures, Lamb waves have received a great deal of attention because they can propagate over considerable distances with little attenuation. Many researchers have investigated Lamb wave propagations and their applications to damage detection [1]–[10]. The conventional Lamb wave based damage detection techniques focus on schemes where the presence

of damage is identified by comparing “current” data with “baseline” data measured at the intact condition of a target structure. However, significant technical challenges exist when realizing this pattern comparison for field applications. For instance, operational and environmental variations of the system such as temperature variation can produce significant changes in the measured signals, masking potential signal changes due to structural damage [11].

To overcome the drawbacks of the conventional NDT methods, a NDT technique, which does not rely on previously obtained baseline data, was proposed by the authors for crack detection [12]. In a thin uniform elastic medium such as an aluminum plate, the formation of a crack causes the propagating Lamb modes to be transformed to other modes. In this previous study, it has been shown that converted Lamb wave modes due to crack formation can be instantaneously extracted using 4 identical lead zirconate titanate (PZT) transducers placed on both sides of the specimen.

In practice, it can be challenging to align PZT transducers on both sides of plates, and the PZT placement can be limited only to a single side of the specimen. The present study was especially motivated by the necessity of attaching transducers only on a single surface of a structure for certain applications such as aircraft. In the present study, the former reference-free damage detection technique is further advanced so that mode conversion due to crack formation still can be identified using only 2 transducers placed on a single surface. For this purpose, a new PZT transducer design called dual PZT transducer is proposed.

This paper is organized as follows. First, a new concept of damage detection using dual PZT transducers is proposed. Next, a reference-free damage classifier that distinguishes signal changes due to crack from initial errors caused by PZT imperfection is proposed. Finally, experimental tests as well as numerical simulations are executed to investigate the applicability of the proposed NDT technique to crack detection.

## II. THEORETICAL BACKGROUND

### A. Theoretical Framework for Crack Detection Using Dual PZT Transducers

In this study, a new design of a dual PZT transducer (hereafter, dual PZT) is conceived so that mode conver-

Manuscript received August 15, 2009; accepted September 24, 2009. This research is supported by the Radiation Technology Program under Korea Science and Engineering Foundation (KOSEF) and the Ministry of Science and Technology (M20703000015-07N0300-01510) and Korea Research Foundation Grant funded by the Korean Government (MOEHRD, Basic Research Promotion Fund) (KRF-2007-331-D00462). Any opinions, findings, and conclusions or recommendations expressed in this material are those of the author(s) and do not necessarily reflect the views of the funding agencies.

H. Sohn is with the Department of Civil and Environmental Engineering, Korea Advanced Institute of Science and Technology, Daejeon, Korea.

S. B. Kim is with the Department of Civil and Environmental Engineering, Carnegie Mellon University, Pittsburgh, PA (e-mail: seungbuk@andrew.cmu.edu).

Digital Object Identifier 10.1109/TUFFC.2010.1401

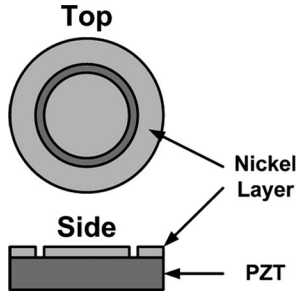


Fig. 1. A schematic drawing of a dual PZT transducer: The dual PZT transducer is fabricated from a circular PZT by etching the top nickel electrode layer into inner circular and outer ring parts.

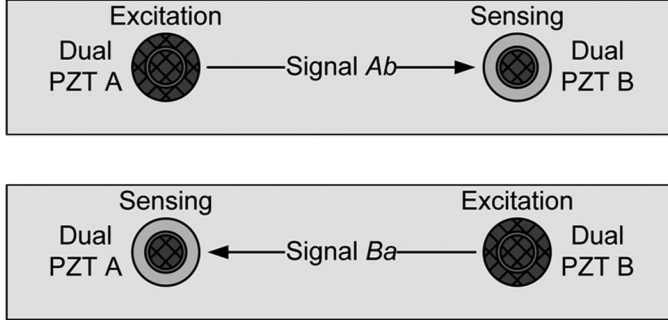


Fig. 2. A schematic diagram of two sets of guided wave signals generated and sensed using two identical dual PZT transducers: Signal  $Ab$  is obtained using both the ring and inner circle parts of dual PZT A (PZT A) as an actuator and the inner circle part of dual PZT B (PZT  $b$ ) as a sensor. Signal  $Ba$  is defined in a similar manner. The patterned areas denote dual PZT parts used for excitation or sensing.

sion due to crack formation can be identified using dual PZTs placed only on a single surface. Fig. 1 illustrates the schematic drawing of a dual PZT. The dual PZT is fabricated from a circular PZT by dividing the top nickel electrode layer into inner circular and outer ring portions through an etching process.

Fig. 2 shows 2 identical dual PZTs (dual PZTs A and B) placed on the top surface of an intact plate. Signal  $Ab$  in Fig. 2 denotes the response signal measured at the inner circle part of dual PZT B (PZT  $b$ ) when the excitation is applied to both the ring and inner circle parts of dual PZT A (PZT A). Signal  $Ba$  is defined in a similar manner (Fig. 2). Here, it is assumed that a narrowband toneburst signal at a specific frequency is used so that only symmetric and antisymmetric zero-order modes ( $S_0$  and  $A_0$  modes) are generated and measured [13].

We first show that signals  $Ab$  and  $Ba$  are identical when damage is not present. To examine this idea, the coupling coefficients of the dual PZT are introduced first. When an excitation voltage is applied to both the ring and inner circle parts (PZT A or PZT B), the coupling coefficients from the electrical energy to the strain energy are defined as  $K_S$  and  $K_A$  for the  $S_0$  and  $A_0$  mode, respectively. Similarly,  $k_S$  and  $k_A$  represent the coupling coefficients of each mode when the input voltage is applied only to the inner circle part (PZT  $a$  or PZT  $b$ ). Note that this coupling coefficient for excitation is identical to the coefficient for

sensing (the coupling coefficient from the strain energy to the electrical energy of the output voltage) [14].

When the amplitudes and shapes of the  $S_0$  and  $A_0$  modes in signals  $Ab$  and  $Ba$  are presented in the frequency domain, the  $S_0$  mode in signal  $Ab$  can be expressed as [15], [16]:

$$k_S(\omega) \cdot m(\omega) \cdot T_S(\omega) \cdot K_S(\omega) \cdot G(\omega) \cdot I(\omega), \quad (1)$$

where  $I(\omega)$  denotes a voltage input applied to the exciting PZT, and  $G(\omega)$  is an electromechanical transfer function at PZT A.  $K_S(\omega)$  represents the coupling coefficient for the  $S_0$  mode at PZT A. In (1),  $K_S$  is used instead of  $K_S^2$  as the coupling coefficient because (1) represents the amplitude and shape of the  $S_0$  mode instead of the energy. Also,  $K_S$  is considered to be frequency dependent in (1).  $T_S(\omega)$  is a structure's transfer function for the  $S_0$  mode and reflects the shape change of the  $S_0$  mode due to Lamb wave dispersion;  $m(\omega)$  is a mechanical-electro transfer function at PZT  $b$ , and  $k_S(\omega)$  is the coupling coefficient for the  $S_0$  mode at PZT  $b$ . Hereafter, the angular frequency  $\omega$  is no longer going to be explicitly shown in the equations and figures for brevity. In a similar fashion, the  $A_0$  mode in signal  $Ab$  can be expressed as  $k_{Am}T_A K_A G I$ , and  $T_A$  denotes the structure's transfer function for the  $A_0$  mode.  $K_A G$  at PZT A and  $k_{Am}$  at PZT  $b$  are the electromechanical and mechanical-electro transfer functions of the  $A_0$  mode, respectively.

Fig. 3 illustrates the schematic diagram of signals  $Ab$  and  $Ba$  in the absence of damage. In Fig. 3, each Lamb wave mode is drawn with its frequency function. Fig. 3 is drawn based on the assumption that the  $S_0$  mode travels faster than the  $A_0$  mode. The arrival times of the  $S_0$  modes in signals  $Ab$  and  $Ba$  are identical because the  $S_0$  mode travels the same distance with the identical speed in both directions. Because the  $S_0$  modes in both signals can be expressed identically in the frequency domain, they have the same amplitudes and shapes in the time domain. In a similar fashion, it can be shown that the  $A_0$  modes in signals  $Ab$  and  $Ba$  are identical (Fig. 3).

Next, the effects of a crack on Lamb wave propagation are discussed. If Lamb waves propagating along a uniform thickness encounter a discontinuity such as a sudden variation in thickness, portions of the waves will be reflected at the discontinuity and the rest will be transmitted through it. When the  $S_0$  mode arrives at a discontinuity as shown in Fig. 4, it is separated into the  $S_0$  and  $A_0$  modes (denoted as  $S_0/S_0$  and  $A_0/S_0$  modes, respectively). Similarly, the  $A_0$  mode is divided into the  $S_0$  and  $A_0$  modes ( $S_0/A_0$  and  $A_0/A_0$  modes) [17], [18].

Fig. 5 illustrates that signals  $Ab$  and  $Ba$  are no longer identical when a crack is introduced. It is assumed in Fig. 5 that the crack is located closer to dual PZT A than to dual PZT B. In Fig. 5, the amplitude ratio of the transmitted but unconverted  $S_0/S_0$  mode to the incident  $S_0$  mode is denoted as  $\alpha$ . Similarly,  $\beta$  denotes the amplitude ratio of the  $A_0/A_0$  mode with respect to the incident  $A_0$  mode. Note that the amplitude ratio of the  $S_0/A_0$  mode

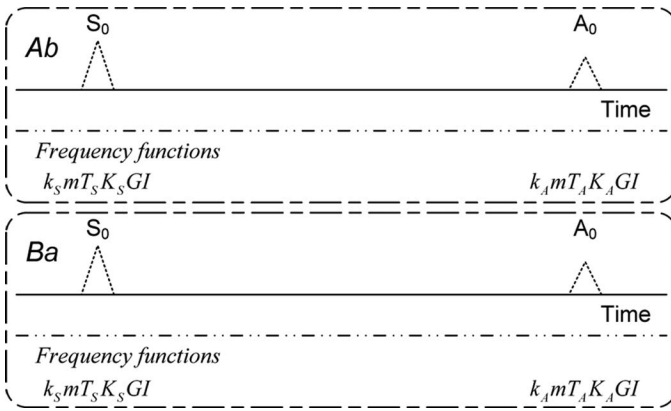


Fig. 3. Comparison between signals  $Ab$  and  $Ba$  in an intact plate: It is shown here that these two signals are identical when damage is absent. Each Lamb wave mode is drawn with its frequency function.  $I$  denotes the voltage input, and  $K_S G$  and  $K_A G$  are the electromechanical transfer functions at PZT  $A$ .  $T_S$  and  $T_A$  are the structure's transfer functions;  $k_S m$  and  $k_A m$  are the mechanical-electro transfer functions at PZT  $b$ . Subscript  $S$  and  $A$  represent the  $S_0$  and  $A_0$  modes, respectively.

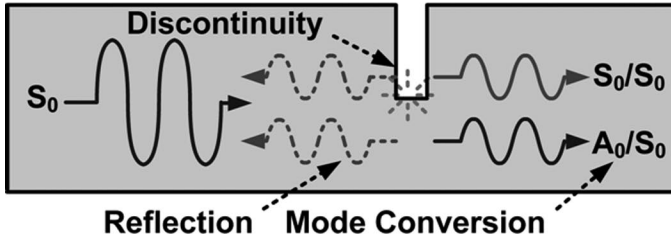


Fig. 4. Generation of mode conversion and reflection due to a discontinuity in a plate with a uniform thickness.

to the  $A_0$  mode is identical to that of the  $A_0/S_0$  mode to the  $S_0$  mode [19]. Hereafter, this amplitude ratio is denoted as  $\gamma$ . To consider the shape changes of the  $S_0/A_0$  and  $A_0/S_0$  modes from the incident  $S_0$  and  $A_0$  modes,  $T_S$  and  $T_A$  are added to their frequency domain expressions, respectively.

After the crack is introduced, signals  $Ab$  and  $Ba$  contain 2 unconverted modes ( $S_0/S_0$  and  $A_0/A_0$  modes) and 2 converted modes ( $S_0/A_0$  and  $A_0/S_0$  modes). As shown in Fig. 5, the  $S_0/S_0$  modes in signals  $Ab$  and  $Ba$  are identical because they have identical frequency functions. In a similar fashion, the  $A_0/A_0$  modes in both signals have identical amplitudes and shapes in the time domain. As for the  $S_0/A_0$  modes in signals  $Ab$  and  $Ba$ , it can be shown that they also have the same amplitudes and shapes. On the other hand, the  $S_0/A_0$  mode in signal  $Ab$  and the  $A_0/S_0$  mode in signal  $Ba$  have different amplitudes although their arrival times and shapes are identical: The frequency function of the  $S_0/A_0$  mode in signal  $Ab$  is  $k_S m T_S \gamma T_A K_A G I$  while that of the  $A_0/S_0$  mode in signal  $Ba$  is  $k_A m T_A \gamma T_S K_S G I$ . In a similar manner, it can be shown that the  $A_0/S_0$  mode in signal  $Ab$  is different from the  $S_0/A_0$  mode in signal  $Ba$ . It should be noted that, when the same size of PZTs are used for excitation and sensing, signals  $Ab$  and  $Ba$  become always identical regardless of the presence of

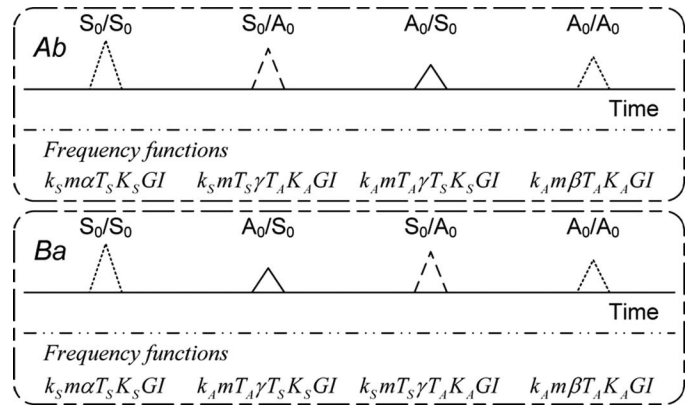


Fig. 5. Comparison between signals  $Ab$  and  $Ba$  in a damaged plate: It is shown that signals  $Ab$  and  $Ba$  are no longer identical as damage appears;  $\alpha$  and  $\beta$  represent the amplitude ratio of the  $S_0/S_0$  mode to the  $S_0$  mode and that of the  $A_0/A_0$  mode to the  $A_0$  mode, respectively;  $\gamma$  denotes the amplitude ratio of the  $S_0/A_0$  mode to the  $A_0$  mode and that of the  $A_0/S_0$  mode to the  $S_0$  mode.

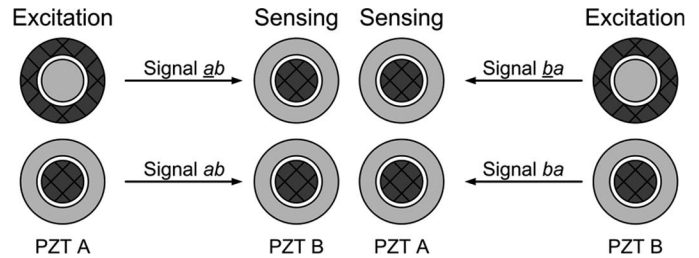


Fig. 6. The notations of various Lamb signals generated and measured using different sizes of PZTs. (Note: Only the patterned areas are activated for excitation or sensing.)

mode conversion ( $K_S m T_S \gamma T_A K_A G I = K_A m T_A \gamma T_S K_S G I$  or  $k_S m T_S \gamma T_A k_A G I = k_A m T_A \gamma T_S k_S G I$ ).

The novelty of the proposed study lies in using different parts of PZTs for Lamb wave generation and sensing. As a result, the presence of mode conversion can be identified simply by examining the difference between signal  $Ab$  and signal  $Ba$ . Furthermore, the findings provided here can be generalized even when additional higher symmetric and antisymmetric modes exist, although only  $S_0$  and  $A_0$  modes are considered in this study.

The previous findings between signals  $Ab$  and  $Ba$  can be extended to other signals pairs shown in Fig. 6. Fig. 6 illustrates the notations of various Lamb signals generated and measured using different parts of dual PZTs. In signal  $ab$ , the outer ring part of PZT A ( $\underline{a}$ ) is excited and the inner circle part of PZT B is ( $\underline{b}$ ) used for measurement. Signal  $ab$  is obtained by exciting the inner circle part of PZT A ( $\underline{a}$ ) and measuring a response from the inner circle part of PZT B ( $\underline{b}$ ). Signals  $\underline{ba}$  and  $\underline{ba}$  are defined in similar manners. As described previously, signals  $\underline{ab}$  differs from signal  $\underline{ba}$  when the damage is present because different parts of dual PZTs are used for excitation and sensing. In contrast, signals  $ab$  and  $ba$  are always identical regardless of damage. (The  $S_0/A_0$  mode in signal  $ab$  matches the  $A_0/S_0$  mode exactly in signal  $ba$  because the same parts

of the dual PZTs are used for actuation and sensing.) As a result, signal  $ab$  contains 2 converted modes that have identical amplitudes and shapes.

Note that Achenbach *et al.* used a similar concept for sensor-self calibration [20]. Also, a similar design of PZT transducers has been developed by Kessler and Shim [21]. They built a self-sensing unit by combining circular and ring type PZT transducers into a single unit. In their transducer unit, the inner circular PZT is exclusively designated for sensing and the ring type PZT is used only for actuation. Furthermore, it operates in a pulse-echo mode. On the other hand, the proposed dual PZT approach allows using varying sizes of PZTs for guided wave generation and measurements, and it operates in a pitch-catch mode.

Because the proposed approach relies on comparison of 2 currently obtained signals rather than comparison with any reference data, this approach is expected to reduce false alarms of defect due to changing operational and environmental conditions such as temperature.

### B. Damage Classification Using Currently Measured Lamb Wave Signals

Here, a new damage classifier is developed to differentiate additional modes caused by damage from the initial errors. In the previous subsection, it is shown that signals  $Ab$  and  $Ba$  are indistinguishable when no damage is present. This is based on the assumptions that the 2 dual PZTs are identical and perfectly bonded to the host structure. In practice, these assumptions cannot be fully satisfied because of variations in dual PZT sizes and bonding conditions. This imperfection in the dual PZTs may produce differences between signals  $Ab$  and  $Ba$  and lead to positive false alarms in the absence of damage. Hereafter, the signal differences resulting from PZT imperfection are referred to as initial errors.

This damage classification scheme is based on the premise that additional modes produced by a defect have unique patterns compared with the initial errors due to PZT imperfection. The proposed technique takes advantage of not only signals  $Ab$  and  $Ba$  but also signals  $\underline{ab}$  and  $\underline{ba}$  for damage classification. The uniqueness of the proposed damage classifier is that damage identification is accomplished using only currently measured signals without relying on pre-stored baseline data or previously established threshold values.

In Fig. 7, the relationship among the Lamb wave signals excited using different parts of dual PZTs is shown. (Note that only different sizes of PZTs are used for excitation, and the same size of the PZT is used for sensing.) In theory, the summation of signals  $\underline{ab}$  and  $ab$  should be identical to signal  $Ab$  for linear elastic waves regardless of crack presence (Fig. 7). In Fig. 8, the relative amplitude and phase information among the Lamb wave signals obtained from the different exciting PZT combinations in Fig. 6 are schematically shown. The Lamb wave signals in Fig. 8 are drawn assuming that there is a crack between

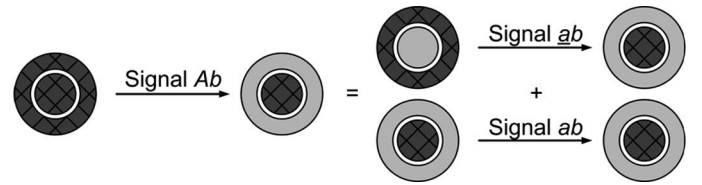


Fig. 7. The relationship among the Lamb wave signals excited using different parts of the dual PZTs.

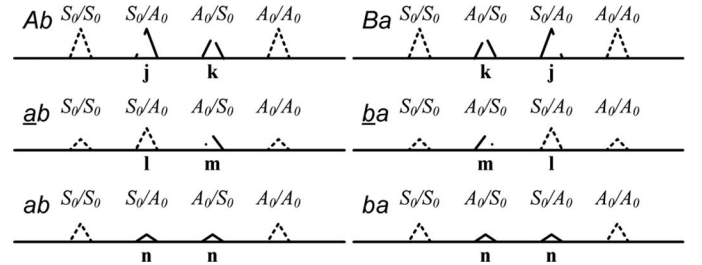


Fig. 8. A schematic diagram of Lamb wave signals excited using different portions of the dual PZT shown in Fig. 2 and Fig. 6. Note: **j**:  $S_0/A_0$  in signal  $Ab$  and  $A_0/S_0$  in signal  $Ba$ ; **k**:  $A_0/S_0$  in signal  $Ab$  and  $S_0/A_0$  in signal  $Ba$ ; **l**:  $S_0/A_0$  in signal  $\underline{ab}$  and  $A_0/S_0$  in signal  $\underline{ba}$ ; **m**:  $A_0/S_0$  in signal  $\underline{ab}$  and  $S_0/A_0$  in signal  $\underline{ba}$ ; and **n**:  $S_0/A_0$  and  $A_0/S_0$  in signals  $ab$  and  $ba$ .

dual PZTs A and B, and it is closer to dual PZT A. The additional modes produced by the crack are denoted as **j**, **k**, **l**, **m**, and **n**. For example, **j** corresponds to the  $S_0/A_0$  mode in signal  $Ab$  and **k** represents the  $A_0/S_0$  mode in signal  $Ba$ .

As described in the previous subsection, the  $S_0/A_0$  and  $A_0/S_0$  modes in signal  $ab$  are identical in terms of the shape and amplitude. Because the summation of signals  $\underline{ab}$  and  $ab$  should be identical to signal  $Ab$ , the  $S_0/A_0$  mode in signal  $Ab$  equals the summation of the corresponding modes in signals  $\underline{ab}$  and  $ab$  (**j** = **l** + **n**). Similarly, the  $A_0/S_0$  mode in signal  $Ab$  is equal to the summation of the  $A_0/S_0$  mode in signal  $\underline{ab}$  and the  $A_0/S_0$  mode in signal  $ab$  (**k** = **m** + **n**). In Fig. 9, it is shown that “signal  $Ab$ –signal  $Ba$ ” (hereafter, signal  $\Delta Ab$ ) is identical to “signal  $\underline{ab}$ –signal  $\underline{ba}$ ” (hereafter, signal  $\Delta \underline{ab}$ ) because “**j** – **l**” equals “**k** – **m**.” Furthermore, the 2 converted modes in signals  $\Delta Ab$  and  $\Delta \underline{ab}$  are symmetric with respect to the middle time point between the arrival times of the  $S_0$  and  $A_0$  modes.

Based on these observations, a reference-free damage classifier is developed. First, signals  $\Delta Ab$  are divided into Window 1 ( $W_1$ ) and Window 2 ( $W_2$ ) as shown in Fig. 9.  $W_1$  starts from the arrival time of the  $S_0$  peak and  $W_2$  ends at the arrival time of the  $A_0$  peak (Fig. 9). The boundary between the 2 time windows is placed in the middle of the  $S_0$  and  $A_0$  peak arrival times. Signal  $\Delta \underline{ab}$  is divided into Window 3 ( $W_3$ ) and Window 4 ( $W_4$ ) in a similar fashion (Fig. 9). By subtracting the signal in  $W_3$  from the corresponding signal in  $W_1$  ( $\Delta W_{13}$ ), the converted mode is removed while the initial errors to PZT imperfection remains. Similarly, “ $W_2 - W_4$ ” ( $\Delta W_{24}$ ) contains only the initial errors.

Next, a damage index (DI) is introduced to measure the closeness between 2 arbitrary signals.

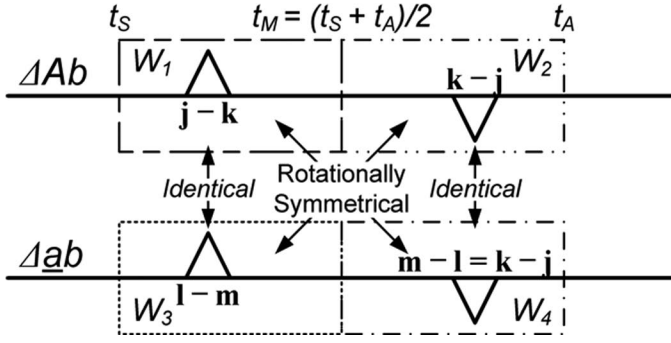


Fig. 9. A schematic diagram of measured signals  $\Delta Ab$  ( $=$  signal  $Ab$   $-$  signal  $Ba$ ) and  $\Delta ab$  ( $=$  signal  $ab$   $-$  signal  $ba$ ): Signals in  $W_1$  are identical to those in  $W_3$  and rotationally symmetrical to the signals in  $W_2$  in the presence of damage;  $t_S$  and  $t_A$  denote the arrival times of the  $S_0$  and  $A_0$  modes, respectively.

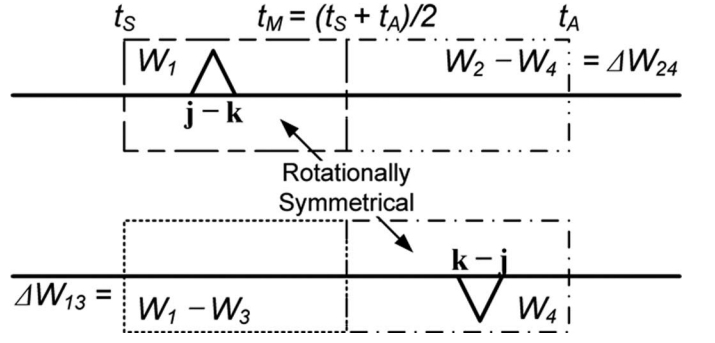


Fig. 10. A schematic diagram of  $W_1$ ,  $\Delta W_{24}$ ,  $\Delta W_{13}$ , and  $W_4$  used to compute the first set of DIs: This first set of DIs is composed of six DIs obtained by comparing all signals in  $W_1$ ,  $\Delta W_{24}$ ,  $\Delta W_{13}$ , and  $W_4$  and DI is defined in Table I.

TABLE I. COMBINATION I: SIX DIs OBTAINED FROM  $W_1$ ,  $\Delta W_{24}$ ,  $\Delta W_{13}$ , AND  $W_4$ .

Damage Index between	
$DI_{1,\Delta 24}$	$W_1$ and " $W_2^T - W_4^T$ " ( $\Delta W_{24}^T$ )
$DI_{1,\Delta 13}$	$W_1$ and " $W_1 - W_3$ " ( $\Delta W_{13}$ )
$DI_{1,4}$	$W_1$ and $W_4^T$
$DI_{\Delta 24,\Delta 13}$	$\Delta W_{24}^T$ and $\Delta W_{13}$
$DI_{\Delta 24,4}$	$\Delta W_{24}^T$ and $W_4^T$
$DI_{\Delta 13,4}$	$\Delta W_{13}$ and $W_4^T$

If  $DI_{1,4}$  is maximum, damage is present.

Superscript T means that the signal is reversed in the time domain before computing DI.

$$DI = \frac{\sqrt{(\sum XY)^2}}{\sqrt{\sum X^2 \sum Y^2}} \times \frac{\min(\sqrt{\sum X^2}, \sqrt{\sum Y^2})}{\max(\sqrt{\sum X^2}, \sqrt{\sum Y^2})}, \quad (2)$$

Shape differences                      Amplitude ratio between two signals

where  $X$  and  $Y$  denote 2 signals being compared. Note that the first term of DI captures only the shape difference between the 2 signals while the second term examines their amplitude difference. DI becomes 1 when the shapes and amplitudes of the 2 signals are identical. As the amplitude and/or shape differences between the 2 signals increase, DI approaches 0. Note that this DI is independent of the signs of the signals. For instance, even if  $X = -Y$ , DI still becomes 1.

In Fig. 10,  $W_1$ ,  $\Delta W_{24}$ ,  $\Delta W_{13}$ , and  $W_4$  are shown. By comparing all signals in these 4 windows, a total of 6 DIs are computed as shown in Table I. Among these 4 windows, only  $W_1$  and  $W_4$  contain converted modes when damage is present (Fig. 10). After reversing  $W_4$  in the time domain ( $W_4^T$ ), it can be shown that  $W_1$  and  $W_4^T$  are fully out of phase (Fig. 10). Therefore, it is expected that DI between  $W_1$  and  $W_4^T$  ( $DI_{1,4}$ ) become the largest value along all 6 DIs when the damage is present. In Table I, superscript "T" represents that the signal is reversed in the time domain. Alternatively, another set of 6 DIs are conceived and presented. (Fig. 11 and Table II). In Combination II, signals in  $\Delta W_{13}$ ,  $W_2$ ,  $W_3$ , and  $\Delta W_{24}$  are used,

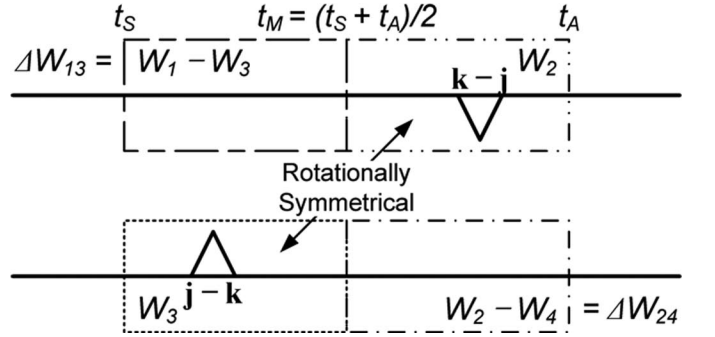


Fig. 11. A schematic diagram of  $\Delta W_{13}$ ,  $W_2$ ,  $W_3$ , and  $\Delta W_{24}$  used to compute the second set of DIs: This second set of DIs is composed of six DIs obtained by comparing all signals in  $\Delta W_{13}$ ,  $W_2$ ,  $W_3$ , and  $\Delta W_{24}$  and DI is defined in Table II.

TABLE II. COMBINATION II: SIX DIs OBTAINED FROM  $\Delta W_{13}$ ,  $W_2$ ,  $W_3$ , AND  $\Delta W_{24}$ .

Damage Index between	
$DI_{\Delta 13,2}$	$\Delta W_{13}$ and $W_2^T$
$DI_{\Delta 13,3}$	$\Delta W_{13}$ and $W_3$
$DI_{\Delta 13,\Delta 24}$	$\Delta W_{13}$ and $\Delta W_{24}^T$
$DI_{2,3}$	$W_2^T$ and $W_3$
$DI_{2,\Delta 24}$	$W_2^T$ and $\Delta W_{24}^T$
$DI_{3,\Delta 24}$	$W_3$ and $\Delta W_{24}^T$

If  $DI_{2,3}$  is maximum, damage is present.

Superscript T means that the signal is reversed in the time domain before computing DI.

and DI between  $W_2^T$  and  $W_3$  ( $DI_{2,3}$ ) should become the maximum value when the damage is present.

Note again that no baseline data are required during this damage classification procedure because damage is identified only using currently measured Lamb wave signals. The proposed damage classifier indicates additional modes caused by damage even in the presence of the initial errors. The applicability of the proposed classification technique is numerically and experimentally validated in the subsequent sections.

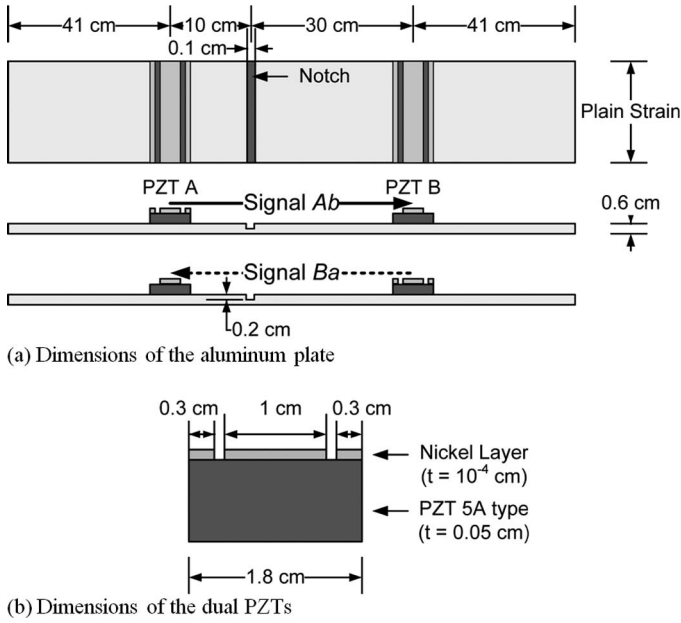


Fig. 12. Dimensions of the aluminum plate and the dual PZTs used in the numerical simulation.

### III. NUMERICAL SIMULATION

The concept of using dual PZTs for crack detection was first validated through numerical simulation. COMSOL 3.4 Multiphysics software ([www.comsol.com](http://www.comsol.com)) was used for the simulation, and Lamb wave propagation in a 2-D aluminum plate was simulated using the combination of plain strain, piezo plain strain, and electrostatics modules in COMSOL software. The length of the plate was 122 cm, and its thickness was 0.6 cm. Two identical dual PZTs were attached to the plate model as shown in Fig. 12. Due to the plain strain assumption of the model, 2-D dual PZTs were also modeled with infinite width as shown in Fig. 12(a). Each PZT patch was divided into outer and inner parts as shown in Fig. 12 (b), and PZT 5A type was used for the numerical study. The thickness of the nickel electrodes and the dual PZT were  $10^{-4}$  cm and 0.05 cm, respectively. The parameter values used in the numerical simulation are listed in Table III. A narrowband toneburst signal at 150 kHz was used as an input signal. In this study, the driving frequency was selected so that only  $S_0$  and  $A_0$  modes could be generated. In the simulation, Rayleigh damping coefficients were set to  $10^{-4}$  for a mass damping coefficient and 0 for a stiffness damping coefficient, respectively. The simulation results were obtained using a time-dependent solver, and a time step was set to 0.25  $\mu$ s, which is equivalent to 4 MS/sec. To control the error in each integration step, relative and absolute tolerances for the solution were chosen to be  $10^{-6}$  and  $10^{-11}$ , respectively. The maximum backward differentiation formula (BDF) order used for setting the degree of the interpolating polynomials in the time-stepping method was set to order 2. Finally, the model was meshed using a mapped mesh option, and the maximum size of each mesh was limited to 1 mm  $\times$  1 mm [22].

TABLE III. PARAMETERS USED IN NUMERICAL SIMULATION.

Exciting frequency	150 kHz
$\alpha$ (Mass damping coefficient)	$10^{-4}$
$\beta$ (Stiffness damping coefficient)	0
Sampling rate	4 MS/s
Relative tolerance	$10^{-6}$
Absolute tolerance	$10^{-11}$
Maximum BDF order	2
Mesh size (mapped mesh)	1 mm $\times$ 1 mm max.

BDF = backward differentiation formula.

Fig. 13 shows 3 pairs of signals, signals  $ab$  and  $ba$ , signals  $\underline{ab}$  and  $\underline{ba}$ , and signals  $Ab$  and  $Ba$ , obtained from the intact condition of the plate. Each pair of signals was practically identical to each other, and it corresponded well to the theoretical expectation. The comparison among signals  $ab$ ,  $\underline{ab}$ , and  $Ab$  in Fig. 13 indicated that the amplitudes of the  $S_0$  and  $A_0$  modes depended on the size of the existing PZT. For instance, both the  $S_0$  and  $A_0$  modes appeared in signals  $ab$  and  $\underline{ab}$  while the  $S_0$  mode was predominant in signal  $Ab$ .

Next, a notch that was 0.2-cm deep and 0.1-cm wide was introduced 10 cm away from PZT A toward PZT B. Even in the presence of the notch, signals  $ab$  and  $ba$  remained identical as shown in Fig. 14(a). However, signal  $\underline{ab}$  became different from signal  $\underline{ba}$  as a result of the mode conversion induced by the notch; see Fig. 14(b). Similarly, the differences between signals  $Ab$  and  $Ba$  became apparent when the damage was present; see Fig. 14(c).

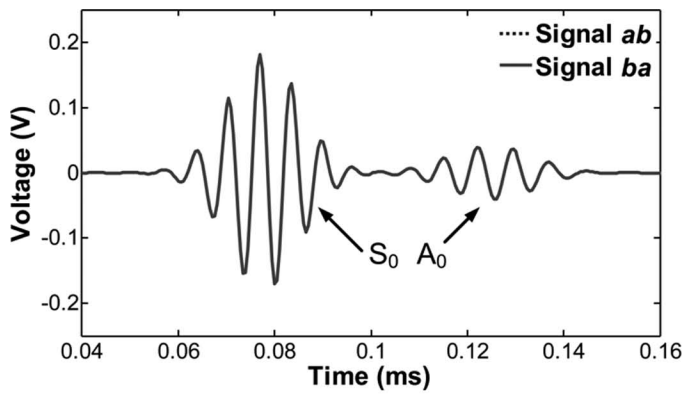
As described in the previous subsection, signal  $\Delta ab$  always should be identical to signal  $\Delta Ab$ . This relationship between signals  $\Delta ab$  and  $\Delta Ab$  was demonstrated in Fig. 15. In the absence of damage, the amplitudes of both signals  $\Delta ab$  and  $\Delta Ab$  were zeros; see Fig. 15(a). On the other hand, converted modes, which are almost identical for signals  $\Delta ab$  and  $\Delta Ab$ , appeared in the presence of damage; see Fig. 15(b). The small discrepancy between 2 signals in Fig. 15(b) is attributed to errors in numerical calculation.

The numerical example presented in this subsection demonstrates the fact that a crack can be identified without relying on previously stored baseline data. The finding in the numerical simulation is further substantiated in the following experimental study.

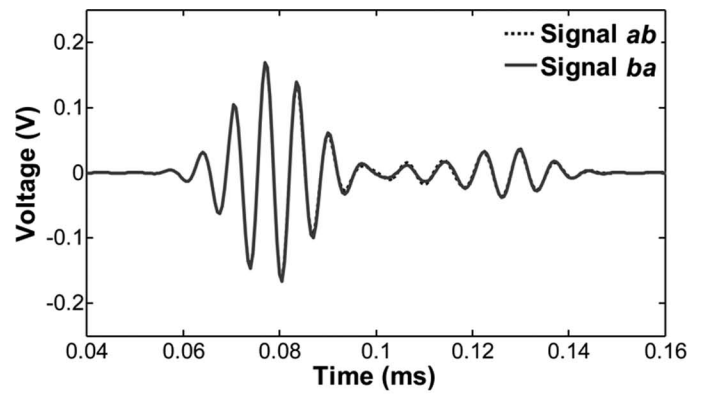
### IV. EXPERIMENTAL RESULTS

#### A. Description of Experimental Setup

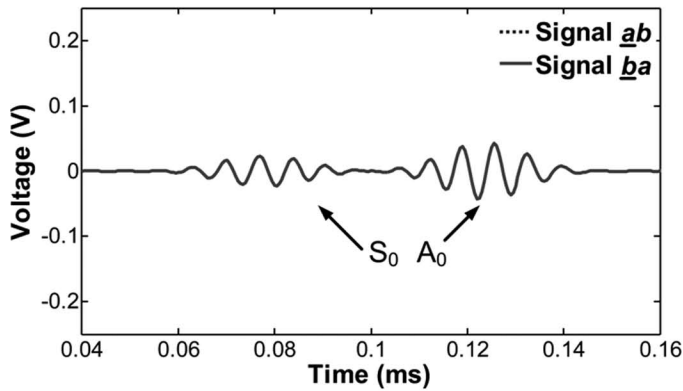
To further examine the proposed reference-free NDT technique, experimental tests have been conducted on an aluminum plate. The overall test configuration and the test specimen are shown in Fig. 16. The data acquisition system was composed of an arbitrary waveform generator (AWG), a high-speed signal digitizer (DIG), a low noise preamplifier (LNP) and a multiplexer (Fig. 16). The dimension of the plate was 122 cm  $\times$  122 cm  $\times$  0.6 cm, and



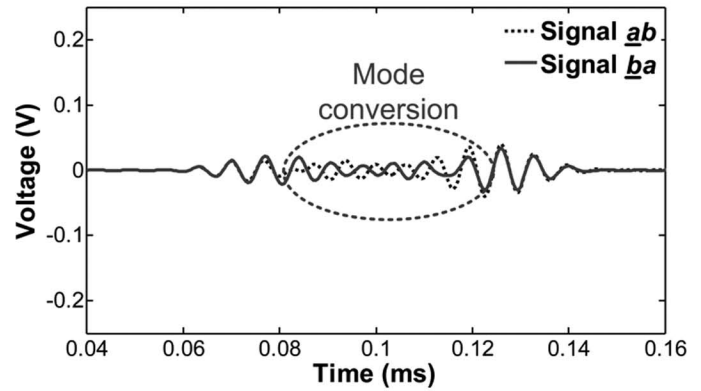
(a)



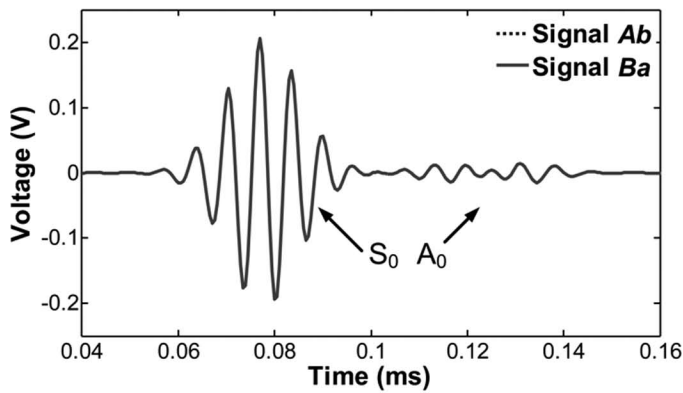
(a)



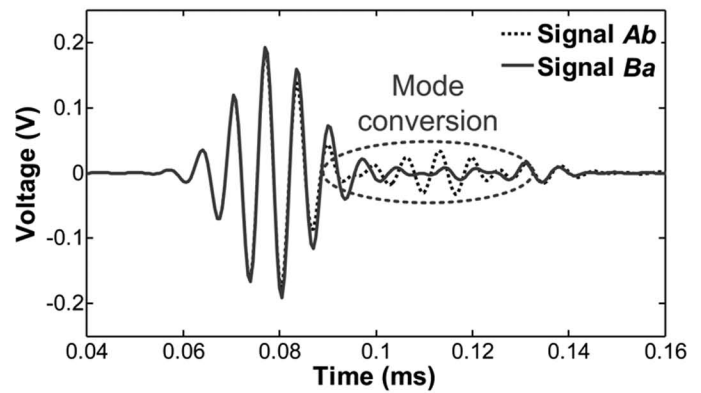
(b)



(b)



(c)



(c)

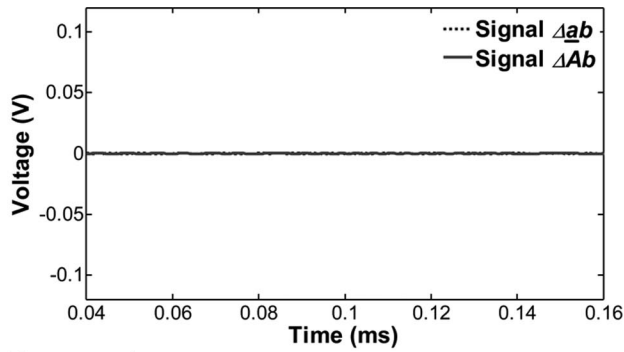
Fig. 13. Three pairs of signals—(a) signals  $ab$  and  $ba$ , (b) signals  $\underline{ab}$  and  $\underline{ba}$ , and (c) signals  $Ab$  and  $Ba$ —simulated from the intact condition of the plate: Each pair of signals was practically identical to the other.

Fig. 14. Three pairs of signals—(a) signals  $ab$  and  $ba$ , (b) signals  $\underline{ab}$  and  $\underline{ba}$ , and (c) signals  $Ab$  and  $Ba$ —simulated with a 2-mm notch: Signals  $\underline{ab}$  and  $\underline{ba}$  (or signals  $Ab$  and  $Ba$ ) are no longer identical.

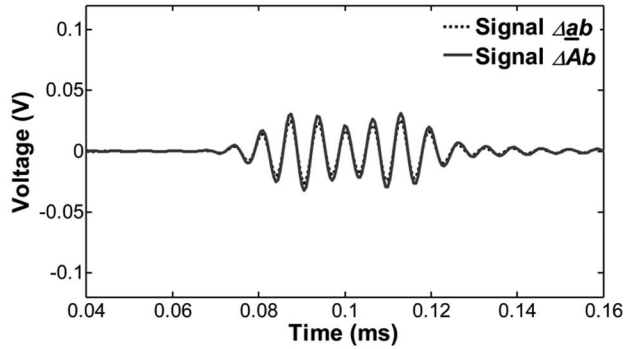
2 circular dual PZTs were mounted in the middle of the plate. PZTs A and B were 40 cm apart each other and attached to the top surface of the plate with commercial cyanoacrylate adhesive. The dual PZT transducer was fabricated by etching the top nickel electrode layer of a PSI-5A4E type PZT wafer transducer into outer and inner parts (diameter of the inner circle: 1.0 cm, diameter of the outer ring: 1.8 cm, and thickness: 0.05 cm) as shown in Fig. 17.

Using the 14-bit AWG, a toneburst signal with a 10 peak-to-peak voltage and a driving frequency of 150 kHz

was generated and applied. First, both ring and inner circle parts of dual PZT A were excited by this input waveform. Then, dual PZT A generated elastic waves and the response was measured at the inner circle part of dual PZT B (signal  $Ab$ ). When the waves arrived at dual PZT B, the voltage output from dual PZT B was amplified by the LNP with a gain of 10 and measured by the DIG. The sampling rate and resolution of the DIG were 20 MS/sec and 16 bits, respectively. To improve the signal-to-noise ratio, the response signals were measured 20 times and averaged in the time domain. After signal  $Ab$  was measured,



(a) Without a notch



(b) With a 2 mm notch

Fig. 15. Comparison of signals  $\Delta ab$  and  $\Delta Ab$  obtained from the undamaged and damaged conditions (numerical simulation).

the same procedure was repeated for signals  $Ba$ ,  $ab$ ,  $ba$ ,  $\underline{ab}$ , and  $\underline{ba}$ , respectively. Detailed test results are described in the following subsection.

### B. Test Results

In Fig. 18, the Lamb wave signals experimentally measured from the intact condition of the specimen are shown. As expected, signals  $ab$  and  $ba$  were practically identical; see Figs. 18(a) and (b). Signals  $\underline{ab}$  and  $\underline{ba}$  in Fig. 18(c) as well as signals  $Ab$  and  $Ba$  in Fig. 18(e) showed small differences even in the absence of damage due to variations in the dual PZTs' size and bonding condition; see Figs. 18(d) and (f).

Next, a 0.15-cm-deep  $\times$  0.1-cm-wide  $\times$  6-cm-long notch was introduced between dual PZTs A and B. The notch was located 10 cm away from PZT A toward PZT B. As a result, 2 additional modes due to mode conversion appeared between the existing  $S_0$  and  $A_0$  modes as shown in Figs. 19(c), (d), (e), and (f), while few differences were found between signals  $ab$  and  $ba$  in Figs. 19(a) and (b).

The test results indicate that mode conversion due to crack can be identified from currently measured Lamb wave signals. In the next subsection, the proposed damage classifier is tested to determine if the identified mode conversion is large enough to indicate an actual defect.

### C. Reference-Free Damage Diagnosis

In Fig. 20, signals  $\Delta ab$  and signals  $\Delta Ab$  obtained from both damaged and undamaged conditions are shown. In

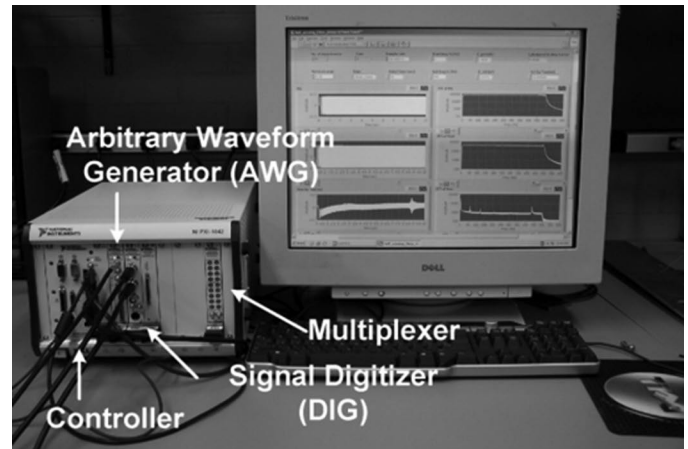


Fig. 16. Test configuration used for validation of the proposed damage detection technique.

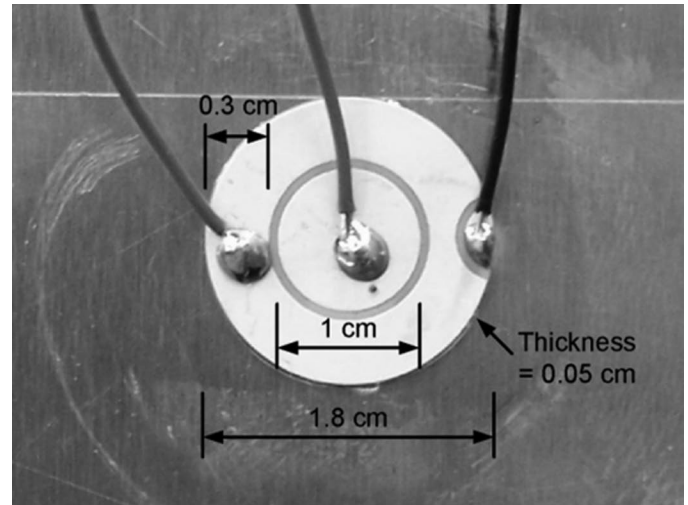


Fig. 17. The dimension of the dual PZT transducer used in this study.

theory, signals  $\Delta ab$  and  $\Delta Ab$  in Fig. 20(a) were supposed to be null signals. In practice, signals  $\Delta ab$  as well as signals  $\Delta Ab$  had some initial errors due to PZT imperfection. Because the sensors have been placed by human operation, different bonding conditions in sensors were unavoidable. As a result, large error signals appear even in the absence of damage.

After the notch was formed, mode conversion was observed in Fig. 20(b). Note that signal difference due to mode conversion was on the same order of the difference without damage. This is because the depth of the formed notch was one quarter of the thickness of the tested aluminum plate. If the depth of the notch is increased, the signal due to mode conversion would have much higher amplitude than the error signal. It also should be noted that signals  $\Delta ab$  and  $\Delta Ab$  are identical for both the undamaged and damaged conditions.

$W_1$ ,  $\Delta W_{24}$ ,  $\Delta W_{13}$ , and  $W_4$  were obtained from signals  $\Delta ab$  and  $\Delta Ab$  according to Combination I described in Table I and Fig. 21, and DIs were calculated using (2). In Fig. 22, 6 DIs obtained according to Combination I



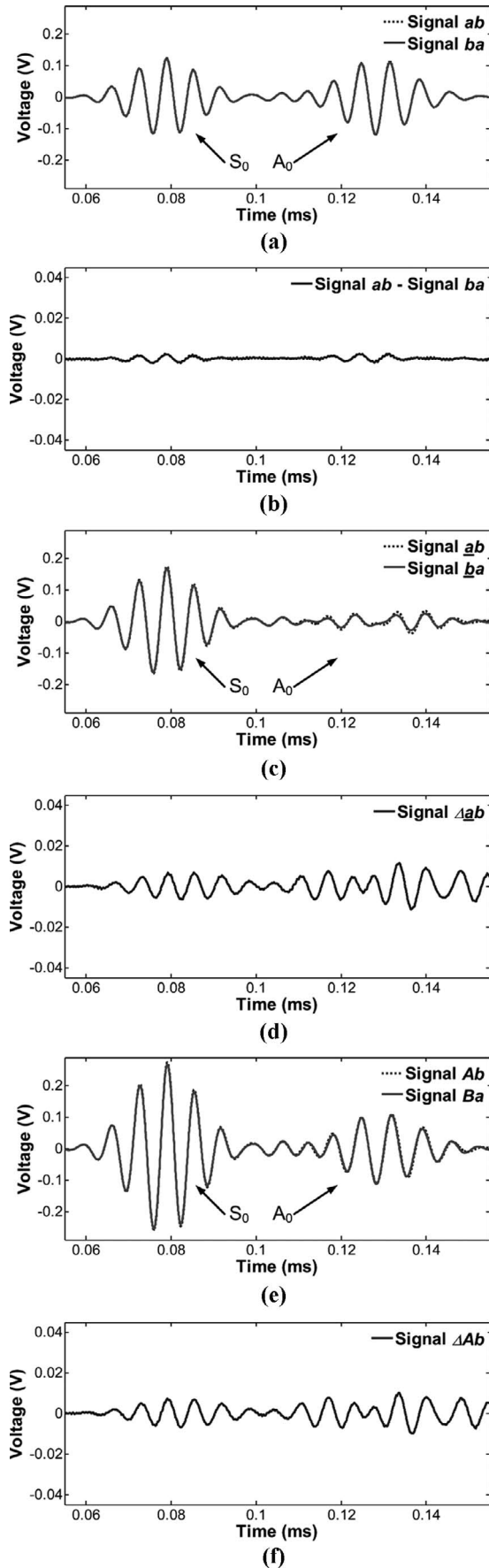


Fig. 18. Measured Lamb wave signals without a notch: (a) signals  $ab$  and  $ba$ , (b) signal  $ab - \text{signal } ba$ , (c) signals  $\underline{a}b$  and  $\underline{b}a$ , (d) signal  $\Delta ab$ , (e) signals  $Ab$  and  $Ba$ , and (f) signal  $\Delta Ab$ .

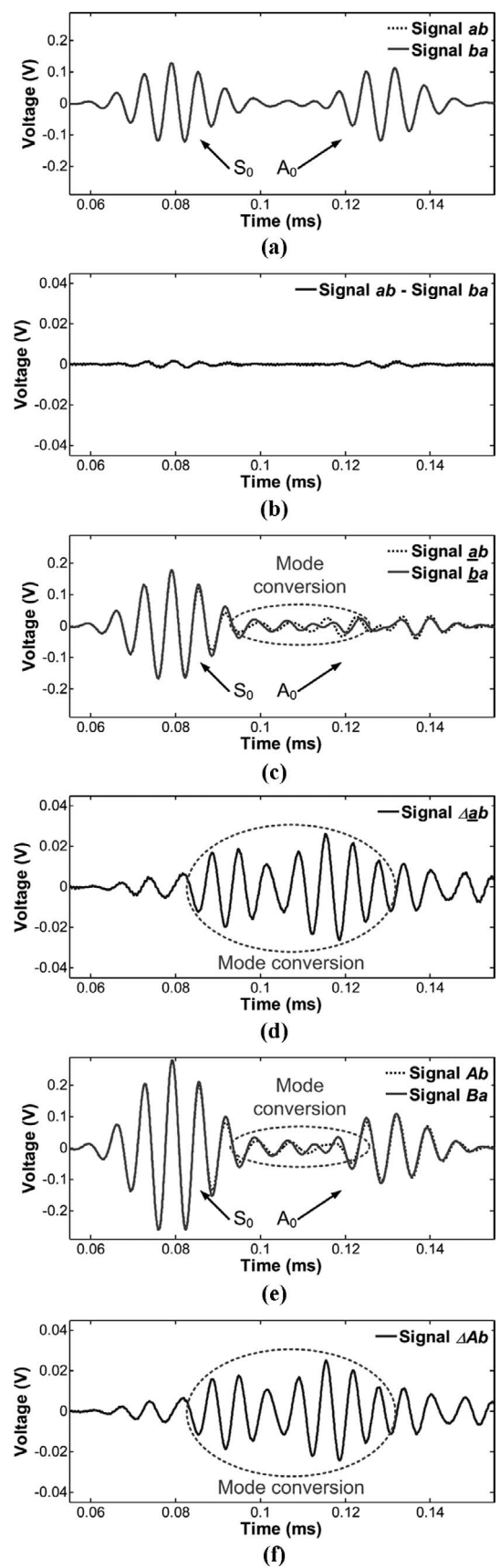


Fig. 19. Measured Lamb wave signals with a 1.5-mm notch: (a) signals  $ab$  and  $ba$ ; (b) signal  $ab - \text{signal } ba$ ; (c) signals  $\underline{a}b$  and  $\underline{b}a$ , mode conversion was found between the  $S_0$  and  $A_0$  modes; (d) signal  $\Delta ab$ ; (e) signals  $Ab$  and  $Ba$ , mode conversion was found between the  $S_0$  and  $A_0$  modes; and (f) signal  $\Delta Ab$ .

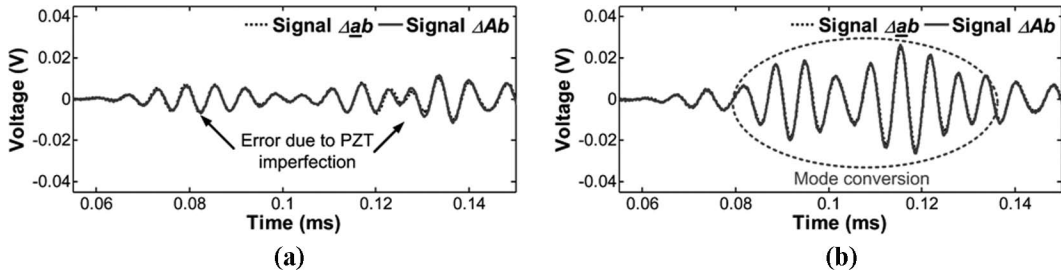


Fig. 20. Comparison of signals  $\Delta ab$  and  $\Delta Ab$  obtained from (a) undamaged and (b) damaged conditions. Damaged condition has a 1.5-mm-deep notch.

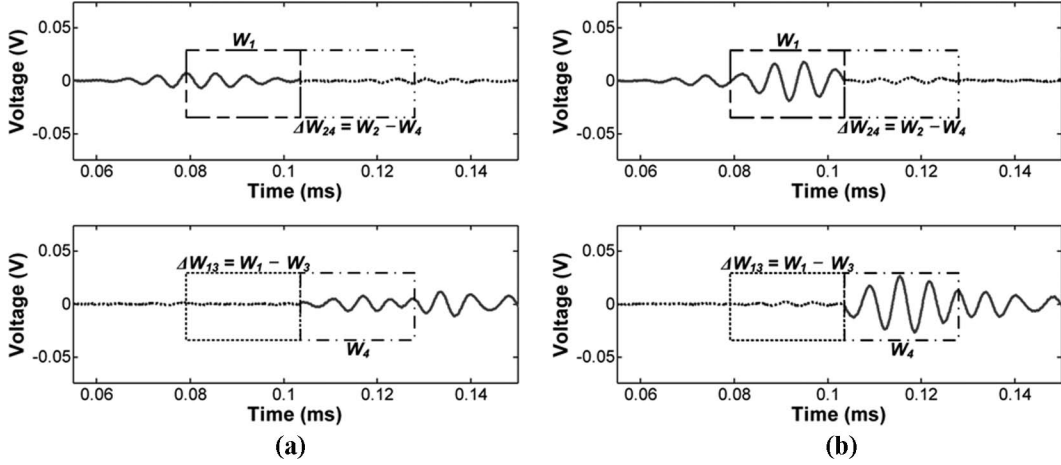


Fig. 21.  $W_1$ ,  $\Delta W_{24}$ ,  $\Delta W_{13}$ , and  $W_4$  obtained from signals  $\Delta Ab$  and  $\Delta ab$  according to Combination I described in Table I and Fig. 10: (a) undamaged condition and (b) damaged condition with a 1.5-mm-deep notch.

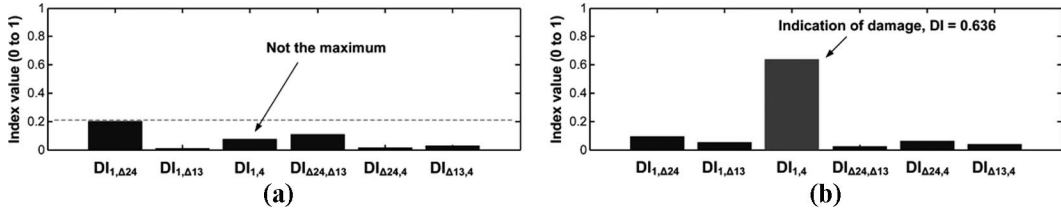


Fig. 22. Reference-free damage classification using DIs obtained according to Combination I shown in Table I (if crack damage existed, the  $DI_{1,4}$  should be the maximum): (a) undamaged condition and (b) damaged condition with a 1.5-mm-deep notch.

are shown for the undamaged and damaged conditions of the plate. In the absence of damage,  $DI_{1,4}$  was not the maximum among the computed DI values. The maximum DI value of 0.203 was found in  $DI_{1,\Delta 24}$ . After the 1.5 mm-deep notch was introduced,  $DI_{1,4}$  became the maximum ( $DI_{1,4} = 0.636$ ). Alternative DIs were calculated based on Combination II and shown in Fig. 23. Without damage, the maximum value, 0.198, was found in  $DI_{3,\Delta 24}$ . With the notch,  $DI_{2,3}$  became the maximum value ( $DI_{2,3} = 0.718$ ) while the second highest was  $DI_{3,\Delta 24}$  (0.084).

Note that conventional techniques require comparison with baseline data to detect a crack or a notch, and their performance may deteriorate under changing operational and environmental conditions. Because the proposed method can perform damage diagnosis without direct comparison with the baseline data, it can complement the conventional techniques.

#### D. Damage Localization

After the presence of the damage was determined, its possible locations were estimated by measuring the arrival time of the converted mode in  $W_1$ . Signal  $\Delta Ab$  contains 2 converted modes,  $S_0/A_0$  and  $A_0/S_0$ , and their arrival times depend on the location of the damage. If the damage is closer to dual PZT A, the  $S_0/A_0$  mode arrives before the  $A_0/S_0$  mode. If the damage is closer to dual PZT B, the  $A_0/S_0$  mode arrives sooner. However, it cannot be determined whether the crack is closer to dual PZT A or dual PZT B based only on signals  $\Delta ab$  and  $\Delta Ab$ . Therefore, 2 possible damage locations are identified by assuming that the converted mode in  $W_1$  is either the  $S_0/A_0$  mode or the  $A_0/S_0$  mode.

Based on the arrival times of the  $S_0$  and  $A_0$  modes in Fig. 20(a), the group velocities of the  $S_0$  ( $V_S$ ) and  $A_0$  modes

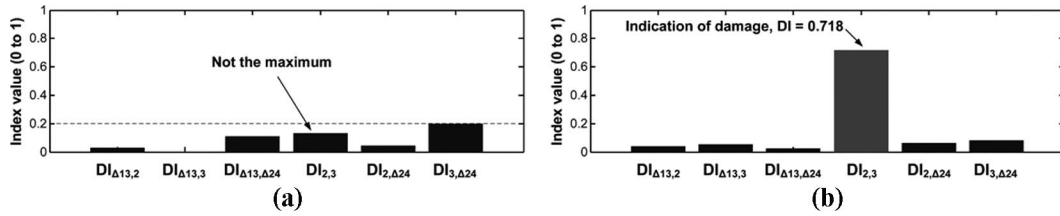


Fig. 23. Reference-free damage classification using DIs obtained according to Combination II shown in Table II (if crack damage existed, the  $DI_{1,4}$  should be the maximum): (a) undamaged condition and (b) damaged condition with a 1.5-mm-deep notch.

( $V_A$ ) were estimated to be 5.063 m/ms and 3.123 m/ms, respectively. They were close to theoretical group velocities,  $V_S = 5.088$  m/ms and  $V_A = 3.055$  m/ms, estimated from the material property. First, one possible damage location was estimated by assuming that the converted mode in  $W_1$  was the  $S_0/A_0$  mode:

$$\text{The arrival time of the converted mode in } W_1 = s/V_A + \left( \text{Distance between PZT A and PZT B} - s \right) / V_S, \quad (3)$$

where  $s$  denotes the distance of the notch from dual PZT A. From the arrival time of the converted mode (0.0918 ms) and (3),  $s$  was estimated to be 10.43 cm. This estimated distance was close to the actual distance (10 cm from dual PZT A, 4.3% error). Another possible damage location was also found by assuming that the converted mode was the  $A_0/S_0$  mode (9.91 cm from dual PZT B toward dual PZT A).

## V. CONCLUSION

In our previous work, an NDT method was proposed so that crack damage in a thin plate structure could be detected without referencing previously stored baseline data. Using 4 identical PZT transducers placed on both sides of the specimen, mode conversion due to damage was clearly extracted. However, attaching the PZT transducers on both sides of the specimen could be a challenging task, and the transducer placement is often limited only on one surface for applications such as aircraft and pipelines.

In this study, the previous reference-free NDT technique is further advanced by introducing a new PZT design named a dual PZT transducer. Using the dual PZT transducer, it is shown that reference-free damage diagnosis can be still achieved by placing 2 dual PZT transducers only on a single surface. The dual PZT is fabricated from a circular PZT by dividing the top nickel electrode layer into inner circular and outer ring portions through an etching process. Then, the presence of crack is instantly detected from the measured Lamb wave signals using the dual PZT transducers. Using dual PZT transducers, multiple Lamb wave signals can be measured in a single wave path and Lamb wave modes due to damage can be extracted from the signals. Furthermore, a new damage classifier was proposed to differentiate converted modes produced by damage from the initial errors caused by PZT imperfection.

Numerical simulations and experimental tests were conducted to validate the effectiveness of the proposed reference-free NDT technique for crack detection. Because this reference-free technique does not rely on previously obtained baseline data for crack detection, it is expected that this approach minimizes false alarms of damage due to changing operational and environmental variations experienced by in-service structures. However, the applicability of the proposed damage detection technique can be affected by sensor imperfections such as improper bonding conditions.

The sensor attachment issue will be closely investigated to reduce error in measurement. The effects of reflections, crack depth, and crack orientation on the PZT transducers on both sides of the plate have been studied in the authors' research group [23]. Similar research will be continued using proposed dual PZT transducers. Further investigation is underway to extend the proposed concept to detection of other types of damage such as delamination and corrosion.

## REFERENCES

- [1] D. N. Alleyne and P. Cawley, "The interaction of Lamb waves with defects," *IEEE Trans. Ultrason. Ferroelectr. Freq. Control*, vol. 39, pp. 381–397, May 1992.
- [2] V. Giurgiutiu, *Structural Health Monitoring with Piezoelectric Wafer Active Sensors*. Boston: Academic Press, 2008.
- [3] P. D. Wilcox, M. J. S. Lowe, and P. Cawley, "Mode and transducer selection for long range Lamb wave inspection," *J. Intell. Mater. Syst. Struct.*, vol. 12, no. 8, pp. 553–565, Aug. 2001.
- [4] D. C. Betz, G. Thursby, B. Culshaw, and W. J. Staszewski, "Structural damage location with fiber bragg grating rosette and Lamb waves," *Struct. Health Monit.*, vol. 6, no. 4, pp. 299–308, 2007.
- [5] W. J. Staszewski, S. G. Pierce, K. Worden, W. R. Philp, G. R. Tomlinson, and B. Culshaw, "Wavelet signal processing for enhanced Lamb-wave defect detection in composite plates using optical fiber detection," *Opt. Eng.*, vol. 36, pp. 1877–1888, Feb. 1997.
- [6] P. Rizzo, M. Cammarata, D. Dutta, H. Sohn, and K. Harries, "An unsupervised learning algorithm for fatigue crack detection in waveguides," *Smart Mater. Struct.*, vol. 18, art. no. 025016, 2009.
- [7] F. B. Cegla, A. Rohde, and M. Veidt, "Analytical prediction and experimental measurement for mode conversion and scattering of plate waves at non-symmetric circular blind holes in isotropic plates," *Wave Motion*, vol. 45, no. 3, pp. 162–177, 2008.
- [8] D. Tuzzeo and F. Lanza di Scalea, "Noncontact air-coupled guided wave ultrasonics for detection of thinning defects in aluminum plates," *Res. Nondestruct. Eval.*, vol. 13, no. 2, pp. 61–78, 2001.
- [9] T. Kundu, S. Banerjee, and K. V. Jata, "An experimental investigation of guided wave propagation in corrugated plates showing stop bands and pass bands," *J. Acoust. Soc. Am.*, vol. 120, no. 3, pp. 1217–1226, 2006.
- [10] S. Banerjee, A. K. Mal, and W. H. Prosser, "Analysis of transient Lamb waves generated by dynamic surface sources in thin composite plates," *J. Acoust. Soc. Am.*, vol. 115, no. 5, pp. 1905–1911, 2004.

- [11] H. Sohn, "Effects of environmental and operational variability on structural health monitoring," Special Issue on Structural Health Monitoring, *Philos. Trans. Royal Soc. A*, vol. 365, no. 1851, pp. 539–560, 2007.
- [12] S. B. Kim and H. Sohn, "Instantaneous reference-free crack detection based on polarization characteristics of piezoelectric materials," *Smart Mater. Struct.*, vol. 16, no. 6, pp. 2375–2387, 2007.
- [13] I. Viktorov, *Rayleigh and Lamb Waves*. New York: Plenum Press, 1967.
- [14] R. C. Buchanan, *Ceramic Materials for Electronics*. New York: Marcel Dekker, 1991.
- [15] C. H. Wang, J. T. Rose, and F. K. Chang, "A synthetic time-reversal imaging method for structural health monitoring," *Smart Mater. Struct.*, vol. 13, no. 2, pp. 415–423, 2004.
- [16] H. W. Park, S. B. Kim, and H. Sohn, "Understanding a time reversal process in Lamb wave propagation," *Wave Motion*, vol. 46, no. 7, pp. 451–467, Nov. 2009.
- [17] S. I. Rokhlin, "Lamb wave interaction with lap-shear adhesive joints: Theory and experiment," *J. Acoust. Soc. Am.*, vol. 89, no. 6, pp. 2758–2765, 1991.
- [18] Y. Cho, "Estimation of ultrasonic guided wave mode conversion in a plate with thickness variation," *IEEE Trans. Ultrason. Ferroelectr. Freq. Control*, vol. 47, pp. 591–603, May 2000.
- [19] W. J. Song, J. L. Rose, J. M. Galan, and R. Abascal, "Ultrasonic guided wave scattering in a plate overlap," *IEEE Trans. Ultrason. Ferroelectr. Freq. Control*, vol. 52, pp. 892–903, May 2005.
- [20] J. D. Achenbach, I. N. Komsky, Y. C. Lee, and Y. C. Angel, "Self-calibrating ultrasonic technique for crack depth measurement," *J. Nondestruct. Eval.*, vol. 11, no. 2, pp. 103–108, Jun. 1992.
- [21] S. S. Kessler and D. J. Shim, "Validation of a Lamb wave-based structural health monitoring system for aircraft applications," in *Proc. SPIE 12th Int. Symp. Smart Structures and Materials*, vol. 5765, 2005, pp. 293–301.
- [22] *COMSOL Multiphysics User's Guide*, COMSOL AB, Stockholm, Sweden, 2005.
- [23] S. H. Park, C. G. Lee, and H. Sohn, "Reference-free crack detection using transfer impedance," *J. Sound Vibrat.*, to be published.



**Hoon Sohn** received the B.S. and M.S. degrees from Seoul National University, Seoul, Korea, and the Ph.D. degree from Stanford University, Stanford, CA, in 1992, 1994, and 1999, respectively, all in civil engineering.

He joined Los Alamos National Laboratory (LANL) as a director-funded postdoctoral fellow (1999–2001), and he was a technical staff member from 2001 to 2004. He joined the faculty of the Civil and Environmental Engineering (CEE) Department, Carnegie Mellon University, Pittsburgh, PA, in August 2004. Currently, he is with the department of CEE at Korea Advanced Institute of Science and Technology (KAIST) as an associate professor. For last fifteen years, his research interest has been in the area of structural health monitoring and sensing technologies. He has published more than 50 refereed journal articles, 150 conference proceedings, and three book chapters. He and his colleagues have been offering a three-day short course entitled "Structural Health Monitoring Using Statistical Pattern Recognition" for the last five years at various locations.

Dr. Sohn won the Best Paper Award at the 2003 SPIE Annual International Symposium on Non-Destructive Evaluation for Health Monitoring and Diagnostics Conference for his paper entitled "Utilizing the Sequential Probability Ratio Test for Building Joint Monitoring." He received the Young Scientists Award from Korean Ministry of Science and Technology with the Presidential Citation and the Incentive Research Grant in 2008.



**Seung Bum Kim** received his B.S. degree in civil, urban, and geosystem engineering from Seoul National University, Seoul, Korea and M.S. degree in civil and environmental engineering (CEE) from Stanford University, Stanford, CA, in 2003 and 2004, respectively.

Currently, he is a Ph.D student in the Department of CEE at Carnegie Mellon University, Pittsburgh, PA, working on developing damage detection techniques for plate structures using piezoelectric transducers.

Mr. Kim won the Best Student Paper Award (1st place) at the World Forum on Smart Materials and Smart Structures Technologies for his paper "Application of an Instantaneous Crack Diagnosis Technique to Thin Metal Plates and Panels" and became the recipient of the Best Student Paper Award (3rd place) at the 6th International Workshop on Structural Health Monitoring for his paper entitled "Instantaneous Crack Detection in Thin Metal Plates and Aircraft Panels."